Available online at www.sciencedirect.com
SCIENCE DIRECT®
Advances in Water Resources 26 (2003) 883–898
Advances in Water Resources
www.elsevier.com/locate/advwatres

Hydraulic conductivity of partially saturated fractured porous media: flow in a cross-section

Dani Or [a,*], Markus Tuller [b,1]

[a] Department of Civil and Environmental Engineering, University of Connecticut, 261 Glenbrook Road, Unit 2037, Storrs, CT 06269-2037, USA
[b] Department of Plant, Soil, and Entomological Sciences, University of Idaho, Moscow, ID 83844-2339, USA

Received 7 October 2002; received in revised form 30 March 2003; accepted 11 April 2003

Abstract

Standard models for hydraulic functions of partially saturated fractured porous media (FPM) often rely on macroscopic continuum representation and embrace constitutive relationships originally developed for homogeneous porous media to describe hydraulic behavior of dual (or multi) continua FPM. Such approaches lead to inconsistencies due to neglect of underlying physical processes governing liquid retention and flow in the vastly different pore spaces. We propose a framework that considers equilibrium liquid configurations in dual continuum pore space as the basis for calculation of liquid saturation and introduction of hydrodynamic considerations. FPM cross-sectional pore space is represented by a bimodal size distribution reflecting two disparate populations of matrix pores and fracture apertures (with rough-walled surfaces). Three laminar flow regimes are considered, flow in: (1) completely liquid filled pore spaces; (2) partially filled pores or grooves bounded by liquid–vapor interfaces; and (3) surface film flow. Assuming that equilibrium liquid–vapor interfaces remain stable under slow laminar flows, sample-scale unsaturated hydraulic conductivity is derived from average velocity expressions for each flow regime weighted by the appropriate liquid-occupied cross-sectional areas (neglecting 3-D network effects). A parameter estimation scheme was developed and evaluated using two data sets. The results point to the critical need for definitive data sets for improved understanding of flow in partially saturated FPM. Hydraulic conductivity functions for non-equilibrium conditions between matrix and fracture domains are discussed. Approximations for inclusion of network effects are proposed based on direct measurement of saturated hydraulic conductivity supplemented by theoretical considerations applying critical path analysis.

1. Introduction

Fractured porous media (FPM) consist of interconnected fracture and pore-networks forming two (or more) distinct pore spaces [24]. Typically, features of sizes in the order of 10^{-4} to 10^{-2} m are associated with fractures [11,33], whereas, the porous matrix contains smaller pore sizes in the range of 10^{-7} to 10^{-5} m [31]. The resulting large disparity in hydraulic behavior between fractures and matrix in partially saturated FPM presents practical and theoretical challenges to modeling of total system response [14,26]. In contrast to relatively well-developed theory and experimental data for flow behavior in saturated FPM, theory and measurements for partially saturated FPM are limited.

Several conceptual models have been proposed to describe liquid behavior within a cross-section of partially saturated fractures (e.g., [19,25,37]). Kwicklis and Healy [16] conducted a numerical study of flow behavior in a simple fracture network considering geometric heterogeneity and air entrapment (matrix was considered impermeable). Their results point to the potential for local spatial variations in pressure heads and fluxes within fractures. Murphy and Thomson [18] examined two-phase flow in a cross-section of fractured porous media focusing on dynamic aspects of multiphase flow and complexity of phase-occupancy and configuration within the cross-section (the medium is represented by a planar lattice model for parallel plate fractures with varying apertures). Recently, Nicholl et al. [19] extended some of these concepts towards derivation of relative permeability functions for partially saturated horizontal

* Corresponding author. Tel.: +1-860-486-2768; fax: +1-860-486-2298.
E-mail addresses: dani@engr.uconn.edu (D. Or), mtuller@uidaho.edu (M. Tuller).
[1] Tel.: +1-208-885-7219; fax: +1-208-885-7760.

0309-1708/03/$ - see front matter © 2003 Elsevier Ltd. All rights reserved.
doi:10.1016/S0309-1708(03)00051-4

Nomenclature

α	dimensionless slit-spacing parameter for matrix pore geometry [20]
β	dimensionless slit-length parameter for matrix pore geometry [20]
γ	pit angle [°]
δ	groove connectivity factor
ε	dimensionless flow resistance parameter for corner flow [21]
η_0	viscosity of bulk liquid [$\mathrm{kg\,m^{-1}\,s^{-1}}$]
λ	slit spacing distribution overlap parameter for matrix pores [20]
μ	matric potential [$\mathrm{J\,kg^{-1}}$]
μ_d	critical matric potential at the onset of matrix pore drainage ($\mathrm{J\,kg^{-1}}$) (air entry value) [20]
μ_1	critical matric potential for the onset of spontaneous fracture drainage [$\mathrm{J\,kg^{-1}}$]
μ_2	critical matric potential for the onset of meniscus recession into surface grooves [$\mathrm{J\,kg^{-1}}$]
ν	dimensionless scaling parameter for fracture element length
ξ	Gamma distribution parameter (set to $\xi = 2$ in this study)
ρ	density of the liquid [$\mathrm{kg\,m^{-3}}$]
σ	surface tension at the liquid–vapor interface [$\mathrm{N\,m^{-1}}$]
ζ	dimensionless flow resistance parameter for flow in isosceles triangular ducts
τ	dimensionless pit-depth scaling parameter for surface grooves
ϕ_F	porosity of the fracture pore space
ϕ_M	porosity of the matrix pore space
ω	Gamma distribution parameter
A_T	total cross-sectional fracture area [$\mathrm{m^2}$]
A_svl	Hamaker constant for solid vapor interactions through intervening liquid (J)
B	fracture aperture size [m]
$B(\mu)$	thin film function to account for modified liquid viscosity close to solid surfaces [35]
$B_1(\mu)$	critical aperture size that separates completely filled and partially filled fractures within the fracture population (integration limit for sample scale expressions) [m]
B_2	critical aperture size that separates fractures with filled and partially filled surface grooves within the fracture population (integration limit for sample scale expressions) [m]
B_cr	critical fracture aperture size based on critical path analysis [m]
B_max	maximum aperture [m]
B_min	minimum aperture [m]
d	dimension of the fracture network (1-D, 2-D, or 3-D)
$f(B)$	aperture distribution
F_γ	angularity factor
g	acceleration of gravity [$\mathrm{m\,s^{-2}}$]
$h(\mu)$	film thickness as a function of matric potential [m]
KS	parallel plate hydraulic conductivity [$\mathrm{m\,s^{-1}}$]
K_s	fluidity term of the parallel plate hydraulic conductivity function [$\mathrm{m^{-1}\,s^{-1}}$]
KD	isosceles triangular duct hydraulic conductivity [$\mathrm{m\,s^{-1}}$]
K_d	fluidity term of the isosceles triangular duct hydraulic conductivity function [$\mathrm{m^{-1}\,s^{-1}}$]
$KF(\mu)$	film hydraulic conductivity [$\mathrm{m\,s^{-1}}$]
$KC(\mu)$	corner hydraulic conductivity [$\mathrm{m\,s^{-1}}$]
K_nw	relative non-wetting phase saturation
K_w	relative wetting phase saturation
K_sat	saturated hydraulic conductivity [$\mathrm{m\,s^{-1}}$]
$K(\mu)$	unsaturated hydraulic conductivity for a unit fracture element [$\mathrm{m\,s^{-1}}$]
$K_\mathrm{u\text{-}F}(\mu)$	upscaled unsaturated hydraulic conductivity for the fracture domain [$\mathrm{m\,s^{-1}}$]
$K_\mathrm{u\text{-}M}(\mu)$	upscaled unsaturated hydraulic conductivity for the matrix domain [$\mathrm{m\,s^{-1}}$]
$K_\mathrm{FPM}(\mu)$	FPM unsaturated hydraulic conductivity [$\mathrm{m\,s^{-1}}$]
P	hydraulic pressure head [m]
p_c	percolation threshold for the fracture network
$r(\mu)$	radius of interface curvature as a function of matric potential [m]
S_w	relative wetting phase saturation
S_1, $S_2(\mu)$, $S_3(\mu)$	relative liquid saturation for a unit fracture element
$S_\mathrm{u\text{-}F}(\mu)$	upscaled relative liquid saturation for a population of fracture elements
$S_\mathrm{u\text{-}M}(\mu)$	upscaled relative liquid saturation for the matrix domain
$S_\mathrm{FPM}(\mu)$	FPM relative liquid saturation
$\overline{v}$	average liquid velocity [$\mathrm{m\,s^{-1}}$]
Z	coordination number (average value) for the fracture network
z	spatial coordinate along flow path [m]

fractures using information of fracture aperture distribution and relative saturation. An alternative to detailed conceptual approaches [18,19,25] invokes macroscopic continuum representation of FPM using parameterization and constitutive relationships developed for homogeneous porous media [17]. However, models based on

such simple representation often fail to capture localized and time-varying flow phenomena [26] leading to inconsistencies in flow behavior due to lack of a physical basis for the choice of effective hydraulic parameters.

In the absence of consensus regarding the spatial scales, flow behavior, and types of pore space heterogeneity amenable to continuum representation [26], there is a clear need for physically sound constitutive relationships between matric potential, liquid retention, and hydraulic conductivity. We propose to assemble such functions for arbitrary pore space geometry using fundamental solid–liquid physical interactions and simplified flow behavior in a cross-section. Such an approach could bridge some gaps between volume-averaged macroscopic representation of flow properties and discrete fracture representation of the FPM, and offer a framework that builds total system response from fundamental physical processes rather than non-physical extension of standard porous media parameters.

The primary objective of this study was to derive constitutive hydraulic functions for FPM from equilibrium liquid configurations as a function of matric potential (μ) within simple and reasonably representative pore space geometry (similar to studies by Pruess and Tsang [25]). The specific objectives were to: (1) propose a conceptual model for FPM pore space geometry; (2) derive closed-form liquid retention functions for matrix and fracture pore spaces (dual-continuum), based on liquid configuration as a function of μ; (3) use equilibrium liquid configurations to introduce hydrodynamic considerations leading to derivation of unsaturated hydraulic conductivity functions for FPM; (4) test the proposed model with available data sets. The main difference between this study and the work of Nicholl et al. [19] is the focus of this work on flow in FPM cross-sections (similar to the "bundle of capillaries") rather than on a detailed account of phase occupancy within a fracture plane (this issue will be discussed in Section 4.4).

The study is organized as follows: In the theoretical section we introduce a unit fracture element for representation of the fracture pore space within the FPM cross-section. Calculated equilibrium liquid–vapor interfacial configurations as a function of matric potential are used to derive the hydraulic conductivity $K(\mu)$ for a two-dimensional (2-D) cross-section of the fracture unit element considering corner, film, and parallel-plate flows. Subsequently, we upscale the unit element results for representation of sample-scale response of the FPM using a statistical distribution of elements and combining flow processes in the two pore domains (matrix and fracture) assuming hydraulic equilibrium. The hydraulic properties of the matrix domain were derived in [35] and are not repeated here. In Section 4, we apply the proposed model using published data. We examine aspects of non-equilibrium between flow domains and their potential effect on the constitutive relationships. Finally, we discuss approximations for inclusion of aspects of 3-D network effects into the proposed 2-D scheme.

2. Theoretical considerations

This section focuses on hydrostatic and hydrodynamic behavior within a two-dimensional representation of rock fracture pore space. The matrix domain hydraulic properties are based on derivations previously reported in [20,34,35]. To avoid duplication we only present a few basic definitions relevant to both, matrix pores and fractures. The basic dimensions of the unit matrix element are depicted in the insert in Fig. 1a.

2.1. Unit fracture element

The 2-D fracture network is represented as an assembly of basic fracture elements; each is comprised of two parallel surfaces separated by a certain aperture size (B). Each surface contains a single groove (or pit) representing surface roughness [21]. The fracture element length (υB), and groove depth (τB), are assumed to be proportional to fracture aperture size (B), as depicted in Fig. 1a. Although such geometrical scaling imposes constraints on the nature of surface roughness, it

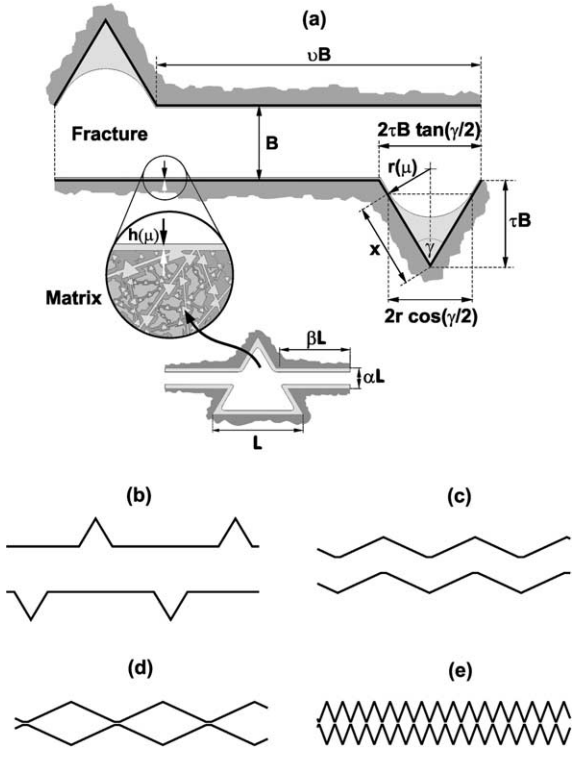

Fig. 1. Definition sketch for (a) a unit fracture element representing a partially saturated fracture with liquid retained in crevices and adsorbed liquid films; (b)–(e) various combinations of scale parameters and surface mating based on the same geometrical definitions as in (a).

simplifies the model and facilitates derivation of closed-form expressions for FPM hydraulic conductivity. Nevertheless, the proposed geometry is reasonably versatile as illustrated in Fig. 1b–e, using several combinations of scale parameters for mated and unmated fracture surfaces. Moreover, scaling constraints can be relaxed as more information on hydraulically relevant surface roughness becomes available [4,5,19].

2.2. Equilibrium liquid configuration within a unit fracture element

Here and in subsequent derivations, we assume thermodynamic equilibrium between fracture and matrix domains (limited experimental evidence lends support for such an assumption, e.g., [37]). Equilibrium liquid–vapor interfacial configurations evolve with changes in matric potential and determine the liquid-occupied cross-sectional areas within a unit fracture element (i.e., saturation). Desaturation of an initially saturated fracture element by a gradual decrease of matric potential may involve spontaneous and rapid liquid displacement and formation of separated interfaces at certain critical potentials, as determined by liquid properties and geometry. Tuller et al. [34] and Or and Tuller [21] show that, for all practical purposes, equilibrium liquid configuration can be determined by a superposition of adsorbed liquid films and capillary held liquid in surface pits and grooves (Fig. 1). The thickness $h(\mu)$ of adsorbed films at a given potential μ is calculated as:

$$h(\mu) = \sqrt[3]{\frac{A_{\mathrm{svl}}}{6\pi\rho\mu}} \tag{1}$$

where A_{svl} is the Hamaker constant, and ρ is liquid density. The radius of interface curvature of a capillary meniscus $r(\mu)$ is calculated for a given potential according to the Young–Laplace equation:

$$r(\mu) = -\frac{\sigma}{\rho\mu} \tag{2}$$

where σ is the liquid–vapor surface tension. Liquid films are assumed to cover all solid surfaces within the unit fracture element; we thus shift the radius of curvature $r(\mu)$ by film thickness $h(\mu)$ to obtain the composite liquid-filled cross-sectional area (see [34] for details of the procedure and associated error analysis).

In the transition from complete saturation (high matric potential) to dry conditions (low matric potential) we distinguish between three filling stages as depicted in Fig. 2.

Starting from a completely saturated unit fracture element and gradually lowering the matric potential to a certain threshold value μ_1 leads to a situation where the fracture spontaneously empties, forming two separate liquid–vapor interfaces on opposite faces of a fracture.

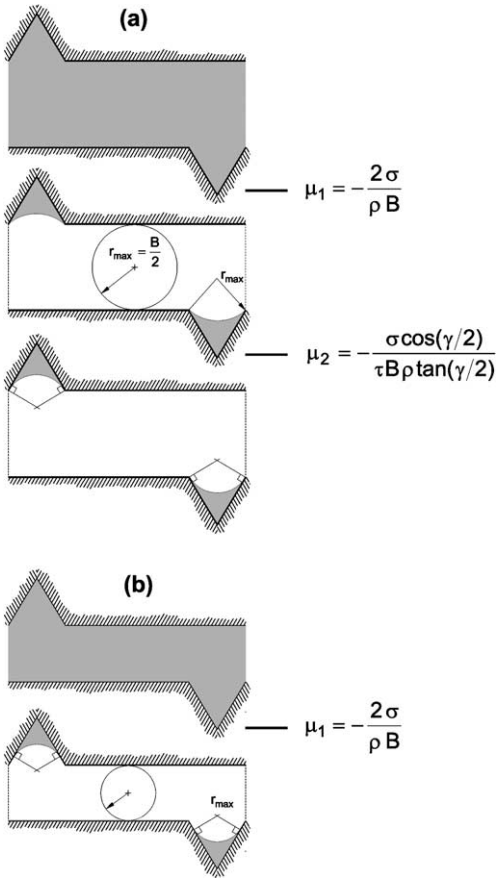

Fig. 2. A sketch illustrating liquid configurations and critical potentials during fracture drainage. (a) Three step transition for geometries where the capillary meniscus is first anchored at the pit edges after interface separation, and then recedes into the surface pit (note that the second transition was introduced for mathematical tractability). (b) Two step transition for geometries where the capillary meniscus immediately tangents the pit walls after interface separation (see text for further details).

The critical potential μ_1 at this point is derived from capillarity considerations:

$$\mu_1 = -\frac{2\sigma}{\rho B} \tag{3}$$

where B is fracture aperture. In the presence of fracture surface roughness some liquid is retained (by capillary forces) in pits and grooves. The radius of interface curvature of a meniscus anchored at the edges of the pit is simply $B/2$ (or $-\sigma/\rho\mu_1$) at the separation potential. For certain pit depths (parameterized by τ) such as,

$$\tau \geqslant \frac{\cos(\gamma/2)}{2\tan(\gamma/2)} \tag{4}$$

the radius of interface curvature at fracture evacuation ($r = B/2$) results in menisci that are tangent to the surfaces of the pit which greatly simplify subsequent calculations. In cases where the inequality in Eq. (4) is not satisfied, we introduce a second potential threshold (μ_2) that marks the starting point for recession of capillary

menisci into the surface pit. The critical potential μ_2 is obtained from simple geometrical considerations:

$$\mu_2 = -\frac{\sigma\cos(\gamma/2)}{\tau B\rho\tan(\gamma/2)} \tag{5}$$

where γ is the pit angle (Fig. 1). Hence, for a given geometry, we first evaluate Eq. (4) and calculate the relevant critical potentials. If the geometry requires introduction of μ_2, the relative saturation curve is obtained by employing the following expressions. For all potentials $\mu > \mu_1$ the unit element is completely saturated and the relative saturation is simply 1.

$$S_1 = 1 \tag{6}$$

Relative saturation is obtained by dividing the liquid occupied cross-sectional area at a given potential by the total cross-sectional area of the unit fracture element, disregarding the associated solid shell (i.e., calculating the fraction of liquid-filled pore space only). For all potentials $\mu_1 \geqslant \mu > \mu_2$ where adsorbed films cover the flat unit element surfaces and capillary menisci are anchored at pit edges, relative saturation is given by:

$$S_2(\mu) = \frac{2\left[Bh(\mu)v - r(\mu)^2\arcsin\left(\frac{B\tau\tan\left(\frac{\gamma}{2}\right)}{r(\mu)}\right) + B\tau\tan\left(\frac{\gamma}{2}\right)\left(B\tau + \sqrt{r(\mu)^2 - \left(B\tau\tan\left(\frac{\gamma}{2}\right)\right)^2}\right)\right]}{B^2\left(v + 2\tau(1+\tau)\tan\left(\frac{\gamma}{2}\right)\right)} \tag{7}$$

where v is a dimensionless fracture length scaling parameter. Note that the denominator in Eq. (7) is the cross-sectional area of a unit fracture element without solid shell. Finally, for all potentials $\mu \leqslant \mu_2$ where a meniscus just recedes into the pit corners and new film covered area is exposed, relative saturation is calculated as:

$$S_3(\mu) = \frac{2h(\mu)\left(Bv + \frac{2\tau B}{\cos\left(\frac{\gamma}{2}\right)} - \frac{2r(\mu)}{\tan\left(\frac{\gamma}{2}\right)}\right) + 2r(\mu)^2F_\gamma}{B^2\left(v + 2\tau(1+\tau)\tan\left(\frac{\gamma}{2}\right)\right)} \tag{8}$$

where F_γ is an angularity (geometrical) factor defined as:

$$F_\gamma = \frac{1}{\tan(\gamma/2)} - \frac{\pi(180-\gamma)}{360} \tag{9}$$

For capillary menisci anchored to groove/pit corners immediately after interface separation (i.e., when Eq. (4) is satisfied), we use Eq. (6) for $\mu > \mu_1$, and Eq. (8) for all potentials $\mu \leqslant \mu_1$. Equilibrium liquid configurations in a unit element cross-section provide the basis for introduction of hydrodynamic considerations for steady flows into the liquid-filled cross-sectional geometry.

2.3. Hydrodynamic considerations within a unit fracture element

A key assumption for consideration of flow processes within a partially saturated FPM cross-section is that equilibrium liquid–vapor interfaces remain stable under relatively slow and laminar flow conditions. Dindoruk and Firoozabadi [8] performed detailed numerical analyses of what they termed "film flow" which is flow bounded by a curved liquid–vapor interface within a partially saturated fracture. Their results show negligible distortion of liquid–vapor interfaces for slow laminar flows characterized by capillary numbers in the range 10^{-6} to 10^{-8}. In accordance with the different liquid filling stages of a unit fracture element discussed in the previous section, we consider four laminar flow regimes (see Fig. 4 below). When the fracture element is completely liquid filled (or saturated), we consider flow between parallel plates (defined by nominal aperture width, B) supplemented by flow in isosceles triangular ducts (surface grooves). For partially filled fracture elements, we invoke the interfacial stability assumption and consider laminar flow in corners (surface grooves) bounded by a liquid–vapor interface, and flow in adsorbed films lining all other fracture surfaces [32]. For the derivation of macroscopic hydraulic conductivity it is not necessary to describe details of the velocity fields; instead, the average flow velocities associated with these flow regimes are sufficient. Solutions of the Navier–Stokes equation for each flow regime and geometry (except for flow in an isosceles triangle given in Appendix A) are discussed in [35].

For completeness, we list the resulting hydraulic conductivities for each flow regime in a unit fracture element derived by substituting average fluid velocity from the Navier–Stokes equation into Darcy's law and considering a unit pressure gradient along the flow path [35]:

Completely liquid-filled cross-section:

$$\text{Parallel plates} \quad KS = K_sB^2 = \frac{\rho g}{\eta_0}\frac{1}{12}B^2 \tag{10}$$

$$\text{Isosceles triangular ducts} \quad KD = K_dB^2 = \frac{\rho g}{\eta_0}\zeta\tau^2B^2 \tag{11}$$

Flow bounded by liquid–vapor interface:

$$\text{Thick film } (h \geqslant 10\text{ nm}) \quad KF(\mu) = \frac{\rho g}{\eta_0}\frac{h(\mu)^2}{3} \tag{12}$$

$$\text{Thin film } (h < 10\text{ nm}) \quad KF(\mu) = \frac{\rho g}{\eta_0}\frac{B(\mu)}{12h(\mu)} \tag{13}$$

$$\text{Corner flow} \quad KC(\mu) = \frac{\rho g}{\eta_0}\frac{r(\mu)^2}{\varepsilon} \tag{14}$$

where ζ and ε are dimensionless flow resistance parameters (ζ is a new result presented in Appendix A), ρ is the density of the liquid, g is the acceleration of gravity, and $B(\mu)$ is a complex function resulting from dependency of fluid viscosity on film thickness in very thin films [21,35].

The hydraulic conductivity of a unit fracture element is then assembled by weighting the hydraulic conductivities of each flow regime by their associated liquid occupied cross-sectional areas and dividing the resulting expressions by the total cross-sectional area of the unit fracture element (including the matrix shell). The total cross-sectional fracture area A_T is simply the fracture area divided by the porosity of the fracture domain ϕ_F:

$$A_T = \frac{B^2\left(v + 2\tau(1+\tau)\tan\left(\frac{\gamma}{2}\right)\right)}{\phi_F} \tag{15}$$

The foregoing analysis yields three new expressions for the hydraulic conductivity of a single unit fracture element at various filling stages given as:

Saturated hydraulic conductivity: $\mu > \mu_1$

$$K_1 = K_{SAT} = \frac{B^4\left(K_s\left(v + 2\tau\tan\left(\frac{\gamma}{2}\right)\right) + K_d 2\tau^2\delta\tan\left(\frac{\gamma}{2}\right)\right)}{A_T} \tag{16}$$

Separated interfaces—capillary menisci anchored at pit edges: $\mu_1 \geqslant \mu > \mu_2$

$$K_2(\mu) = \frac{KF(\mu)2vBh(\mu) + KC(\mu)\delta\left(2\tau B\tan\left(\frac{\gamma}{2}\right)\left(\tau B + \sqrt{r(\mu)^2 - \tau^2B^2\tan\left(\frac{\gamma}{2}\right)^2}\right) - 2r(\mu)^2\arcsin\left(\frac{\tau B\tan\left(\frac{\gamma}{2}\right)}{r(\mu)}\right)\right)}{A_T} \tag{17}$$

Separated interfaces—capillary menisci tangent pit surfaces: $\mu \leqslant \mu_2$

$$K_3(\mu) = \frac{2KF(\mu)h(\mu)\left(Bv + \frac{2B\tau}{\cos\left(\frac{\gamma}{2}\right)} - \frac{2r(\mu)}{\tan\left(\frac{\gamma}{2}\right)}\right) + 2KC(\mu)\delta r(\mu)^2F_\gamma}{A_T} \tag{18}$$

where K_s, K_d, $KF(\mu)$, and $KC(\mu)$ are the basic hydraulic conductivities given in Eqs. (10)–(14) (see also Fig. 4), and $0 < \delta < 1$ is a groove connectivity factor to account for partial groove or pit connectivity in the direction of flow [21]. The parameter δ ensures that isolated pits do not contribute to the hydraulic conductivity functions in Eqs. (16)–(18).

For fracture geometry that satisfies the inequality in Eq. (4), we use Eq. (16) for $\mu > \mu_1$, and Eq. (18) for all matric potentials $\mu \leqslant \mu_1$. Note that employing $KC(\mu)$ Eq. (14) in Eq. (17) leads to a slight underestimation of $K_2(\mu)$ within the narrow matric potential range from μ_1 to μ_2 that may be neglected for all practical purposes.

A framework similar to the one described here was instrumental in deriving pore scale expressions for liquid retention and hydraulic conductivity for matrix pore space comprised of angular central pores connected to slit-shaped spaces (see [20,35]).

2.4. Upscaling considerations

For representation of FPM hydraulic properties at the sample scale, we employ a statistical upscaling scheme that assumes a bimodal distribution for matrix pore sizes and fracture apertures accounting for the two disparate pore populations and porosity as depicted in Fig. 3.

The individual contributions of matrix pores and fractures to liquid saturation and unsaturated hydraulic conductivity are calculated separately, using the appropriate pore sizes and aperture distributions. The resultant saturation curves are weighted by the porosities of the respective domains and summed up to obtain the composite medium response. A similar approach was taken by Wang and Narasimhan [37] in their Eqs. (7.3.3) and (7.3.4) to represent the composite liquid retention and hydraulic conductivity functions for the fracture and matrix domains.

To avoid duplication with matrix domain derivations, we briefly explain the upscaling scheme for the fracture domain. We employ a statistical gamma distribution to represent the positive skewness often observed in fracture aperture size distributions [3,6,11,25,37]. The gamma density function is dependent on two parameters ξ and ω [28]:

$$f(B) = \frac{B^\xi}{\xi!\omega^{\xi+1}}\exp\left(-\frac{B}{\omega}\right) \quad B \geqslant 0 \tag{19}$$

where B is the fracture aperture, and the parameter ξ is limited to integer values. To facilitate derivation of analytical solutions that involve expectations of $f(B)$, we have used a fixed value $\xi = 2$ that provided the right balance between flexibility of the expressions and mathematical tractability.

Sample-scale expressions for liquid saturation and unsaturated hydraulic conductivity are obtained by taking expectations or integrating pore scale expressions (Eqs. (6)–(8) for liquid saturation, and Eqs. (16)–(18) for unsaturated hydraulic conductivity) with the gamma

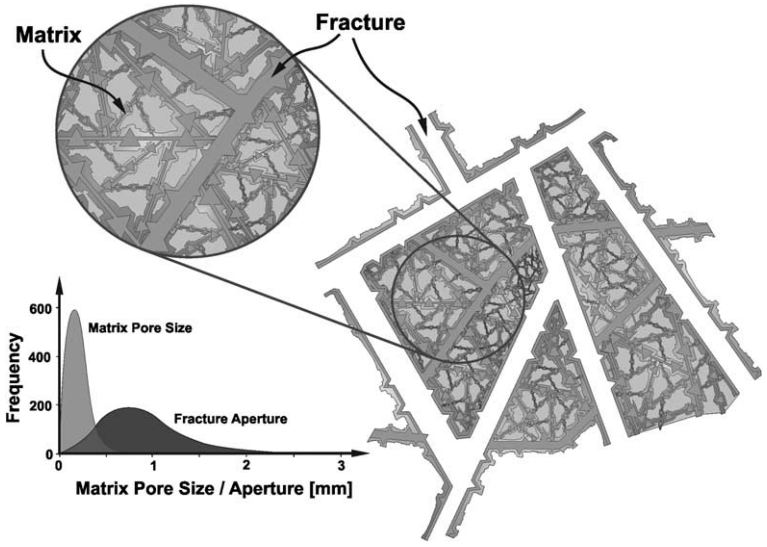

Fig. 3. Conceptual sketch for dual continuum pore space representation of a FPM. The matrix is represented by angular pores connected to slit-shaped spaces. Note (1) the pore size disparity between the two domains; and (2) large fractures empty first.

distribution Eq. (19) over portions of the fracture population associated with the different filling stages discussed in Section 2.2. The integration limits separating the fracture population are obtained by rearranging Eqs. (3) and (5) and solving for the fracture apertures $B_1(\mu)$ and B_2 that define the fracture size separation between different filling stages at a given potential (see Fig. 4). Individual contributions of each fracture group in the population at a given potential are summed. The process is repeated for the entire matric potential range under consideration to yield the sample-scale saturation and hydraulic conductivity curves.

In the following example we illustrate the derivation of upscaled hydraulic conductivity (i.e., taking the expectation integral) for the fraction of the aperture population that is completely liquid filled (in the size range from smallest aperture $B_{\min}$ to $B_1(\mu)$ in Fig. 4):

$$K_{1u\text{-}F}(\mu) = \int_{B_{\min}}^{B_1(\mu)} \overbrace{\left[\frac{B^4(K_s(v + 2\tau\tan(\gamma/2)) + 2K_d\tau^2\tan(\gamma/2))}{A_T}\right]}^{K_1 \text{ for a single fracture element Eq. (16)}} \overbrace{\left[\frac{B^2}{2\omega^3}\exp\left(-\frac{B}{\omega}\right)\right]}^{\text{Gamma distribution with } \xi=2} \mathrm{d}B \tag{20}$$

with subscript u denoting "upscaled", and F for "fracture". Note that the saturated hydraulic conductivity for the entire fracture domain can be readily calculated using Eq. (20) by simply changing the upper limit of integration to maximum aperture size $B_{\max}$. The same procedure is applied to Eqs. (17) and (18) with integration limits $B_1(\mu)$ to B_2, and B_2 to $B_{\max}$, respectively. The upscaled expressions are then added to yield the composite response for the entire fracture population at a particular matric potential.

$$K_{u\text{-}F}(\mu) = \overbrace{K_{1u\text{-}F}(\mu)}^{\text{Eq. (20)}} + \overbrace{K_{2u\text{-}F}(\mu)}^{\text{upscaled Eq. (17)}} + \overbrace{K_{3u\text{-}F}(\mu)}^{\text{upscaled Eq. (18)}} \tag{21}$$

For geometrical configurations with pit scaling parameters $\tau \geqslant \cos(\gamma/2)/(2\tan(\gamma/2))$ Eq. (4), the upscaled expressions can be solved analytically as shown in Appendix B. Note that these analytical solutions cover a wide variety of different geometrical configurations. Only cases with $\tau < \cos(\gamma/2)/(2\tan(\gamma/2))$ require numerical evaluation of the upscaled expressions (Fig. 5).

The same scheme applies for liquid saturation Eqs. (6)–(8), with the composite response of the entire population calculated as:

$$S_{u\text{-}F}(\mu) = \overbrace{S_{1u\text{-}F}(\mu)}^{\text{upscaled Eq. (6)}} + \overbrace{S_{2u\text{-}F}(\mu)}^{\text{upscaled Eq. (7)}} + \overbrace{S_{3u\text{-}F}(\mu)}^{\text{upscaled Eq. (8)}} \tag{22}$$

Note that the contribution of completely liquid-filled fractures $S_{1u\text{-}F}(\mu)$ is obtained by simply integrating the gamma distribution Eq. (19) between the limits $B_{\min}$ and $B_1(\mu)$, since the relative saturation of a saturated fracture element is 1.

For the matrix domain we employ a similar upscaling scheme yielding $S_{u\text{-}M}(\mu)$ and $K_{u\text{-}M}(\mu)$ [20,35]. The individual contributions of the matrix and fracture domains to liquid saturation are added and weighed by the porosities of the individual domains to obtain the composite saturation curve for the FPM:

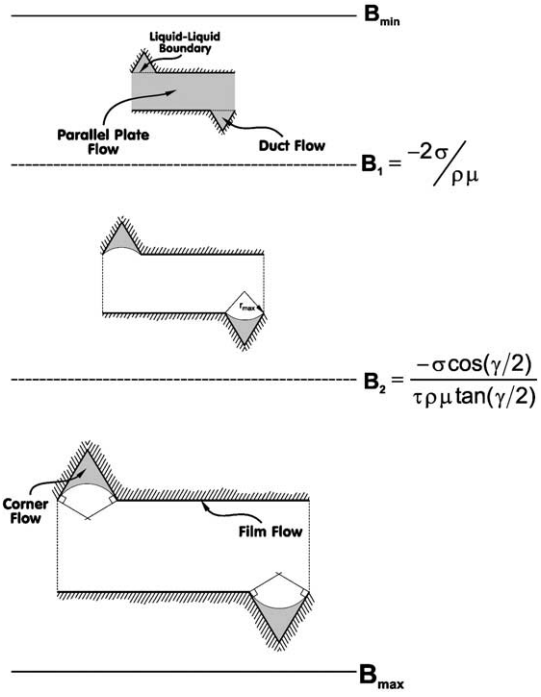

Fig. 4. Critical aperture sizes determining expected fracture-filling stages at different matric potentials.

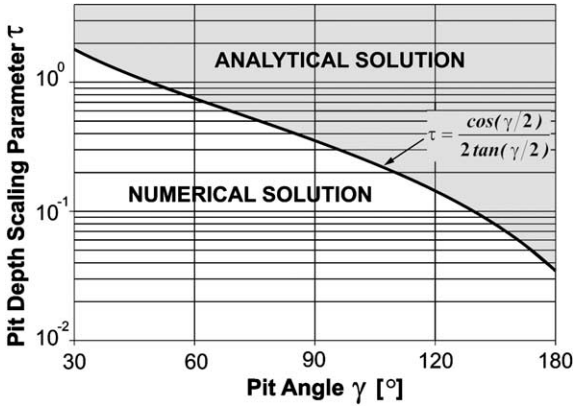

Fig. 5. Relationship between pit angle and pit depth scaling parameter separating analytical and numerical solutions for the proposed sample scale expressions for liquid saturation and hydraulic conductivity.

$$S_{\mathrm{FPM}}(\mu) = \frac{S_{\mathrm{u\text{-}M}}(\mu)\phi_{\mathrm{M}} + S_{\mathrm{u\text{-}F}}(\mu)\phi_{\mathrm{F}}}{\phi_{\mathrm{M}} + \phi_{\mathrm{F}}} \tag{23}$$

where ϕ_{M} and ϕ_{F} are the matrix and fracture porosities. The composite hydraulic conductivity curve is obtained by simple addition of the individual contributions of the matrix and fracture domains that are already normalized by their respective porosities (i.e., the individual expressions are already divided by total cross-sectional areas):

$$K_{\mathrm{FPM}}(\mu) = K_{\mathrm{u\text{-}M}}(\mu) + K_{\mathrm{u\text{-}F}}(\mu) \tag{24}$$

Obviously the upscaling scheme presented here involves vast simplifications such as the assumption of parallel pathways, hence the neglect of the fully three-dimensional nature of the fracture network and complexities associated with phase interference discussed by Persoff and Pruess [23], and by Murphy and Thomson [18].

3. Model application

3.1. Estimation of model parameters

The analytical sample-scale expressions for the matrix and fracture domains contain model parameters that can be either estimated from direct measurements or via model fitting to measured hydraulic properties (e.g., saturated hydraulic conductivity).

If the aperture distribution is known from measurements (such as image analyses or hydrodynamic characterization), only four model parameters are needed to describe saturation and hydraulic conductivity functions for the fracture domain. These parameters are directly related to fracture geometry, namely: dimensionless fracture lengths and pit depth scaling parameters v and τ, pit connectivity factor δ, and pit angle γ. The number of parameters can be further reduced or constrained when information regarding fracture geometry becomes available (e.g., groove angle or spacing [4,5]).

The model for the matrix domain requires four additional geometrical parameters [35]: a dimensionless slit length parameter β (Fig. 1a), the gamma distribution parameter ω (see Section 2.4), the matric potential μ_{d} at air entry (characterizes largest pore size $L_{\max}$), and a distribution overlap parameter λ relating slit spacing α to largest $L_{\max}$ [20]. These model parameters are estimated by fitting to measured liquid retention data, while matching medium specific surface area and porosity. The dimensionless parameter β determines the slit length of the unit matrix element (Fig. 1a), and is highly dependent on measured matrix specific surface area [34]. The potential at the onset of drainage μ_{d} (air entry value) is often attributed to the largest pore size present in the porous medium, which we denote as $L_{\max}$, and is estimated as one of the fitting parameters. The distribution overlap parameter λ relates the dimensionless slit spacing parameter α (Fig. 1a) to largest ($L_{\max}$) and mean $m(L)$ pore lengths ($\alpha = m(L)/(L_{\max}\lambda)$) to determine the largest slit aperture (or the leading edge of slit-spacing distribution). According to this relationship, increasing the parameter λ results in a decrease in overlap and smaller slit spacing (for a detailed discussion please see [20]).

The resulting model parameters describe the saturation curve and are subsequently used to predict unsaturated hydraulic conductivity [35]. A conceptual flow

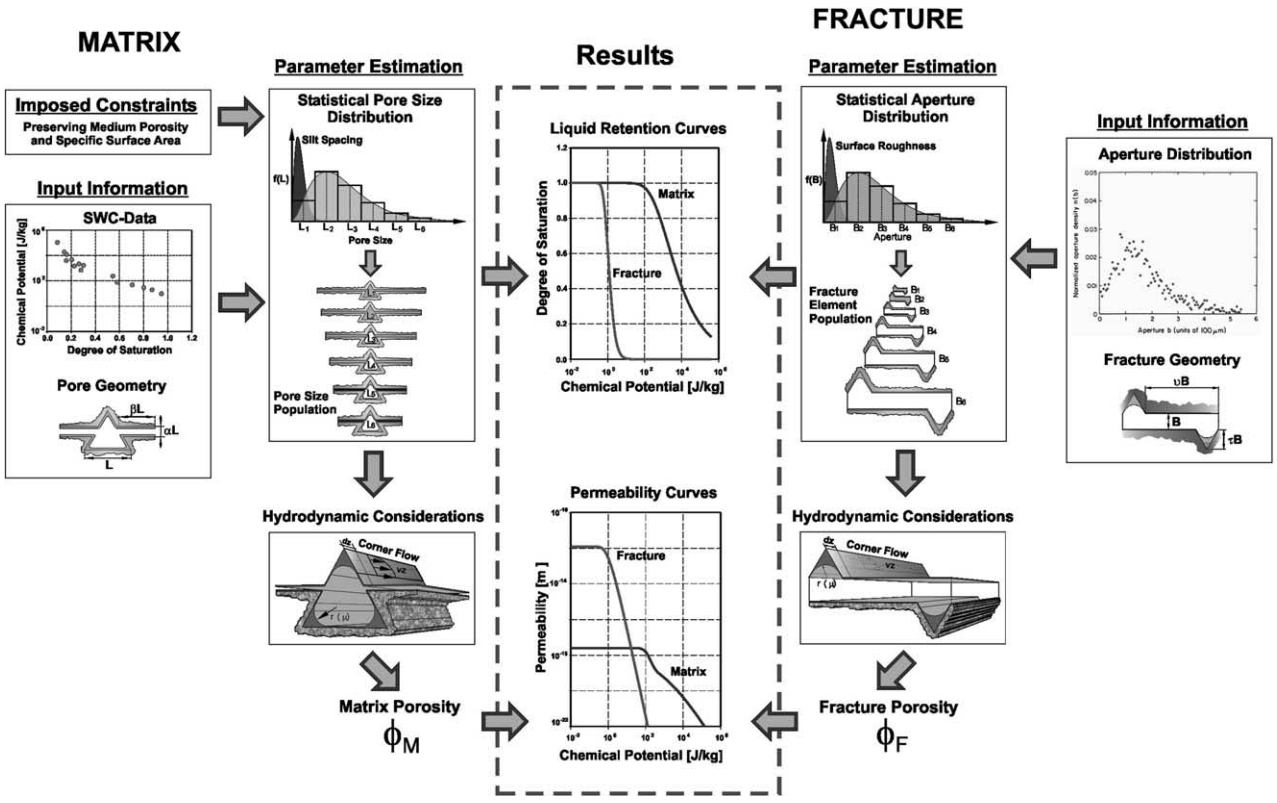

Fig. 6. A conceptual flow chart of the parameter estimation scheme. Assumed matrix pore geometry and measured matrix liquid retention data are used as input parameters to estimate free matrix model parameters while imposing surface area and porosity constraints, resulting in liquid saturation and hydraulic conductivity. Assumed fracture geometry and measured aperture size distribution in combination with fracture porosity and saturated fracture permeability are used to determine fracture model parameters for calculating the continuous liquid saturation curve and predicting fracture hydraulic conductivity as a function of matric potential. Note that the individual contributions of the matrix and fracture domains are superimposed and weighted by matrix and fracture porosities to receive the composite response of the FPM.

chart of the proposed parameter estimation scheme is depicted in Fig. 6.

3.2. Datasets

Datasets containing information on matrix and fracture liquid retention and unsaturated permeability, as well as other physical properties of the two domains, are virtually non-existent. A comprehensive search of relevant literature spanning the last few decades yielded only a few incomplete datasets suitable to test the proposed model. In the following, we use data for Tiva Canyon welded tuff reported by Wang and Narasimhan [37] to illustrate the primary features of the proposed model, and a dataset for crystalline rock reported by researchers at the Swiss Federal Institute of Technology (SFIT) [11,13] for model applications.

The Tiva Canyon welded tuff (TCwt) dataset [37] contains information about matrix porosity, saturated matrix and fracture permeabilities, van Genuchten [36] parameters α_{VG} and n_{VG} for the matrix liquid—saturation matric potential relationship (water characteristic curve), and fracture spacing and effective aperture for vertical fractures. Fracture porosity for a unit volume is calculated by dividing the effective aperture by aperture spacing. The shape of the aperture distribution is approximated with the gamma distribution Eq. (19) with $\xi = 2$ and B_{min} and B_{max} set to values of 1×10^{-9} and 5×10^{-4} m, respectively. The second gamma distribution shape parameter ω is calculated, based on the assumption that the critical aperture size (discussed below) is equal to the mean of the distribution $m(B) = \omega(\xi + 1)$. Reported and derived model input parameters for TCwt are listed in Table 1.

The SFIT dataset [11,13] is for a sample from a fracture zone at Grimsel Test Site (Switzerland) [11] with granodiorite rock matrix. This dataset contains measured water characteristic and gas permeability data, saturated matrix and fracture permeabilities, matrix and fracture porosities, and aperture size distribution. Gas permeability measurements obtained at various water saturations were converted to equivalent water permeability to be useful for model evaluation using the following parametric van Genuchten Mualem relationship [10].

$$K_{nw}(S_w) = (1 - S_w)^{0.5}(1 - S_w^{1/m})^{2m} \quad (25)$$

Table 1
Reported and derived model input parameters for the TCwt and SFIT datasets

Property	TCwt[a]	SFIT[b]
Matrix porosity	1.14×10^{-1}	3.75×10^{-2}
Matrix α_{VG} [J/kg]$^{-1}$	8.40×10^{-4}	NA
Matrix n_{VG}	1.558	NA
Matrix saturated permeability [m^2]	2.55×10^{-18}	3.00×10^{-18}
Effective aperture [m]	1.09×10^{-3}	NA
Aperture spacing [m]	0.180	NA
Fracture porosity	6.10×10^{-4}	8.50×10^{-3}
Fracture saturated permeability [m^2]	1.18×10^{-12}	3.00×10^{-13}
Aperture distribution parameter $\omega(\xi=2)$ [m]	3.30×10^{-5}	2.10×10^{-4}
Minimum aperture B_{min} [m]	1.00×10^{-9}	6.00×10^{-8}
Maximum aperture B_{max} [m]	5.00×10^{-4}	4.00×10^{-3}

NA is not applicable.
[a] Source is [37].
[b] Source is [11,13].

where K_{nw} is the relative non-wetting phase (gas) permeability, S_w is the relative wetting phase (water) saturation, and m is the empirical van Genuchten shape parameter. The shape parameter m obtained from fitting Eq. (25) to measured K_{nw} data was subsequently used to calculate the relative wetting phase (water) permeability K_w as:

$$K_w(S_w) = S_w^{0.5}[1-(1-S_w^{1/m})^m]^2 \tag{26}$$

The conversion from non-wetting phase to wetting phase permeability for the SFIT data is depicted in Fig. 7. Reported SFIT data are listed in Table 1. Physical constants used in the illustrative calculations are listed in Table 2.

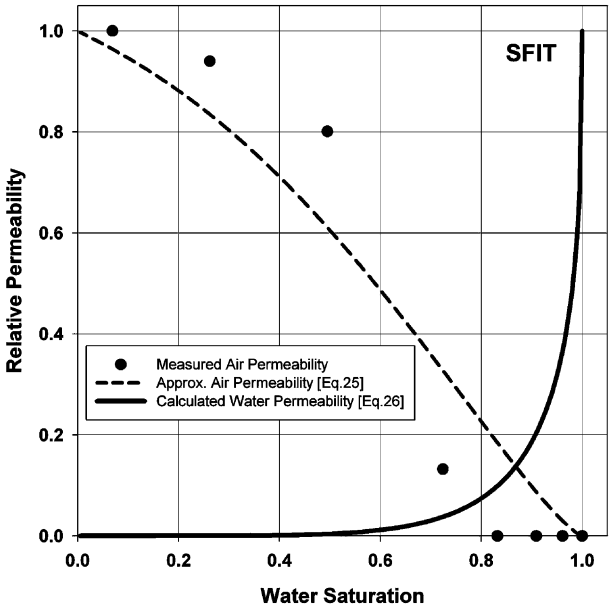

Fig. 7. Conversion of non-wetting to wetting phase permeabilities for the SFIT dataset.

4. Results and discussion

4.1. Tiva Canyon data set [37]

The lack of complete and definitive data sets for model testing introduces undesired degrees of freedom into the evaluation. We thus view the use of the Tiva Canyon welded tuff data [37] as an illustrative example rather than a test of model validity in the strict sense. Input parameters used in the scheme illustrated in Fig. 6 are given in Table 1. Fig. 8a depicts the resulting water characteristic curves for matrix and the fracture domains (note the fracture domain is seen on the bottom left corner of Fig. 8a). As expected, the matrix domain dominates the saturation-matric potential relationships. In contrast, the permeability function (Fig. 8b) is dominated by the fracture domain at low matric potentials (close to complete saturation). The transition between fracture- to matrix-dominated permeability occurs at a potential of about −50 J/kg. A second transition occurs at potentials of −2000 J/kg, where matrix film flow

Table 2
Physical constants and dimensions used in the illustrative example calculations

Property	Symbol		Unit
Acceleration of gravity	g	9.81	m s^{-2}
Density of water (20 °C)	ρ	998.21	kg m^{-3}
Hamaker constant (solid–vapor through liquid)	A_{svl}	-6.0×10^{-20}	J
Surface tension of water (20 °C)	σ	0.0728	N m^{-1}
Viscosity of water (20 °C)	η_0	0.001002	kg m^{-1} s^{-1}

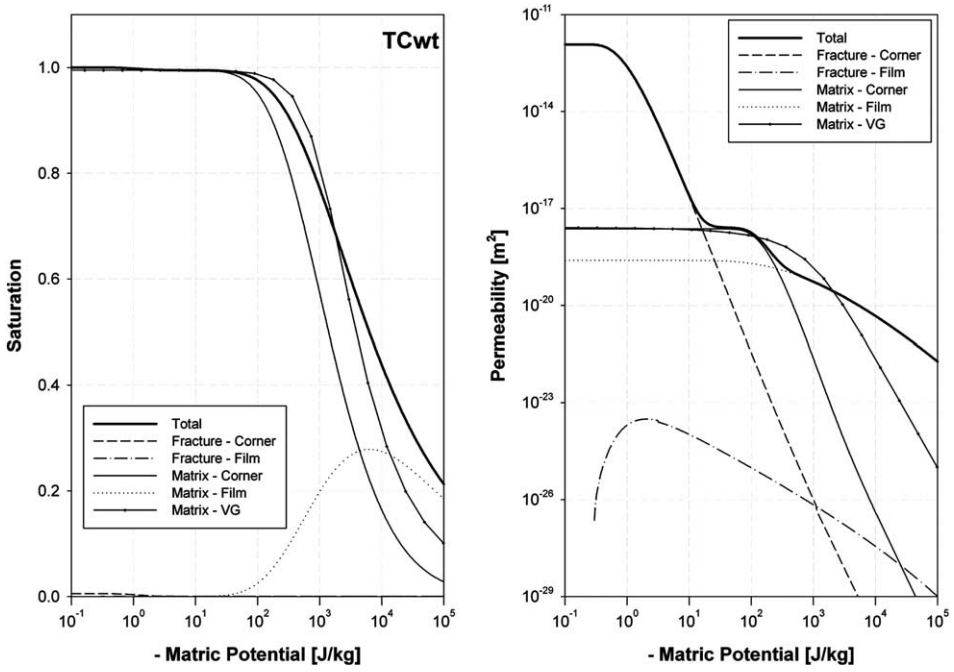

Fig. 8. Calculated saturation and predicted permeability curves for the Tiva Canyon welded tuff unit. Note the corner and film flow contributions within the matrix and fracture domains.

provides the dominant contribution to the overall FPM permeability. The resulting unsaturated permeability curve contains three ''humps''—one for each of these processes. It is interesting to note that fracture film flow provides only a marginal contribution to transport processes, probably due to the limited exposed fracture surface area (i.e., few and mostly small aperture-size fractures). Finally, all model-fitting parameters are summarized in Table 3.

4.2. SFIT data set [11,13]

The SFIT data set was less complete than the previous Tiva Canyon data set. Following a similar path, we present the model fit to water characteristic data (Fig. 9a) for matrix and fracture domains. The resulting fracture size distribution is then used to predict the unsaturated hydraulic conductivity function. The resulting function manifests the influences of the various domains and mechanisms, namely the dominance of the fracture domain near saturation, a transition to matrix corner and capillary flow, and finally, matrix film flow ($\mu \approx -2000$ to -3000 J/kg) [35]. Model parameters for SFIT are given in Table 3. Attempts to use the fracture aperture distribution reported by Fischer et al. [11] failed to reproduce either saturation or permeability values. One possibility for this discrepancy is the fact that the fractures were filled with porous material [11], hence, in terms of our model, a fracture size distribution with a smaller mean was needed to reproduce measured hydraulic functions.

Table 3
Fitted model parameters for the TCwt and SFIT datasets

Datasets	TCwt	SFIT
Matrix model parameters[a]		
Slit length scaling parameter β	80,000	10
Pore size distribution parameter ω [m]	6.1×10^{-7}	2.8×10^{-7}
Matric potential μ_d at the onset of drainage [m]	−3.5	−5.0
Distribution overlap parameter λ	57	15
Fracture model parameters		
Fracture length scaling parameter υ	5	10
Pit depth scaling parameter τ[b]	8.0×10^{-1}	3.5×10^{-2}
Pit connectivity factor δ	0.3	1.0
Pit angle γ [°]	60	150

[a] See [20].

[b] The pit depth scaling parameter was set to $\tau \geqslant \cos(\gamma/2)/(2\tan(\gamma/2))$ to facilitate analytical solutions.

4.3. Hydraulic conductivity function for non-equilibrium conditions

Thus far, the analyses and resulting hydraulic conductivity functions were based on the assumption of hydraulic equilibrium between matrix and fracture domains. There is considerable interest in hydraulic functions for situations where matrix and fractures are not in equilibrium, such as due to arrival of a rapid wetting front from a rainfall event via preferential pathways or ventilation of the fracture domain [17,30]. We should clarify that details regarding rates and amounts of liquid exchange between these domains are usually not addressed in standard medium characterization. These

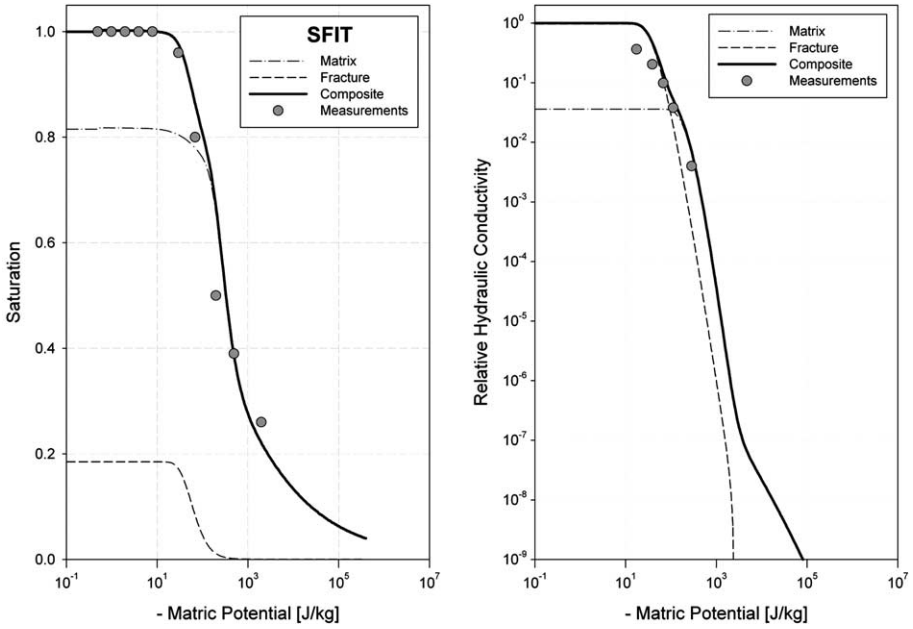

Fig. 9. Calculated saturation and predicted permeability curves for the SFIT dataset compared to measured data.

questions lie in the realm of solution of a particular flow problem rather than medium characterization often requiring standardized steady state conditions. Nevertheless, under certain non-equilibrium conditions when mass exchange between the domains is ignored (e.g., due to relatively long time scale for imbibition relative to rapid downward flow [17]), we may assemble a generic unsaturated permeability function for different values of potential differential ($\Delta\mu$). For the example depicted in Fig. 10, we assume that the matrix domain is wetter than the fracture domain ($\Delta\mu = \mu_{\text{matrix}} - \mu_{\text{fracture}} > 0$). Under these conditions, for each value of matrix permeability at a given potential μ, we calculate fracture domain permeability at $\mu + \Delta\mu$ and combine the contributions according to Eq. (24) (with the assumption of parallel pathways). The resulting family of permeability curves (Fig. 10) reflects the dependency of overall FPM permeability on the "distance" from equilibrium ($\Delta\mu$) up to the potential difference value where no flow through the fracture domain occurs (i.e., $\Delta\mu > 20$ J/kg) which also coincides with the matric potential value marking the transition to matrix-dominated permeability ($\mu \approx -20$ J/kg). The situation where the fracture domain is wetter than the matrix is trivial, due to the large disparity in permeability near saturation; the composite permeability function will not be significantly different than the original equilibrium case. Kwicklis and Healy [16] presented results similar to Fig. 10 (their Fig. 12) in the equivalent continuum representation of permeability of networks with different fracture aperture sizes (small and large size networks resemble our matrix and fracture domains, respectively).

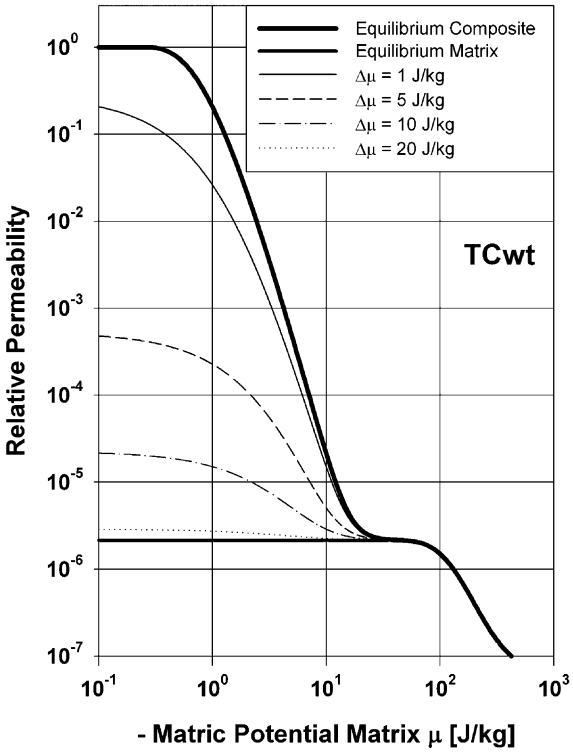

Fig. 10. Permeability curves for TCwt under non-equilibrium conditions.

4.4. Simple approximations for three-dimensional network effects

An obvious limitation of the foregoing analysis is the description of hydraulic properties for a two-dimen-

sional (2-D) cross-section, neglecting potentially important three-dimensional (3-D) network effects (network connectivity and phase interference). Two relatively simple approaches are proposed for incorporation of 3-D influences into the 2D model. The first is to measure the saturated hydraulic conductivity or permeability of the FPM and use it as input parameter to constraint model parameters. Such a measurement, which presumably incorporates the 3-D nature (connectivity) of the fracture network, will provide constraints for estimation of geometrical distribution of aperture sizes. We envision that the resulting fracture aperture distribution will be a 2-D equivalent that faithfully preserves the 3-D hydrodynamics (for fully saturated conditions). In the absence of detailed information regarding fracture size distribution, we have tested this approach for the Tiva Canyon data set (TCwt).

Alternatively, a theoretical approach based on concepts of critical path analysis (CPA) from percolation theory [1,2,12,15] is proposed. The implementation of CPA in this context is based on the following argument; given a broad aperture distribution forming a 3-D fracture network, we begin by removing all the fractures, and then replace the fracture segments in order of decreasing size back to their original location. The aperture size that completes a conductive pathway across the network is labeled as the "critical" aperture size. According to CPA, all aperture sizes larger than the "critical" are essentially in series (all flow must pass through the "critical" size), and all aperture sizes smaller than the "critical" size could be in parallel but are much less conductive, thus providing a limited contribution to the overall hydraulic conductivity. Consequently, the hydraulic conductivity of the fracture network can be represented by the hydraulic conductivity of the "critical" unit fracture element. The critical fracture size is determined by finding the cumulative fraction of fracture sizes larger than the critical size (B_{cr}) that equals the percolation threshold of the network (p_c):

$$p_c = \int_{B_{cr}}^{\infty} f(B)\,\mathrm{d}B \tag{27}$$

The percolation threshold is the minimal fraction of aperture sizes that span a conductive pathway, and its value depends mainly on the dimensionality of the network ($d = 1$, 2, or 3) and on the coordination number, Z. For simple cubic lattices $p_c = 0.2488$; other values may be estimated as [29]:

$$Zp_c \cong \frac{d}{d-1} \tag{28}$$

The value of the coordination number Z is difficult to determine a priori, however, evidence suggests that for diluted fracture networks (and soil macropore networks), Z values close to 3 are common [9,22,29]. Hence, for $Z = 3$ in a 3-D fracture network, the value of $p_c = 0.5$ and the critical aperture size is equal to the mean value of the aperture size distribution. The value of B_{cr} can be used to estimate the saturated hydraulic conductivity of a unit fracture element (using Eq. (16)) to represent the entire fracture domain and the FPM. Performing this calculation (3-D network, $Z = 3$, $p_c = 0.5$) for the SFIT dataset yields a K_{SAT} of 4.6×10^{-15} m^2, compared to 6.1×10^{-15} m^2 calculated with Eq. (20). Although such a match should be regarded with caution, it illustrates the potential usefulness of the CPA in using univariate distribution of fracture apertures to obtain an estimate for network K_{SAT} [12,15].

In summary, we propose to constrain our estimates of fracture size distribution such that the calculated planar (2-D) saturated hydraulic conductivity will match the 3-D estimated from the critical aperture identified by CPA. This could be an iterative process constrained by other input parameters, such as measured saturated hydraulic conductivity.

5. Summary and conclusions

The large disparity in hydraulic behavior between fracture and matrix domains in partially saturated FPM presents a challenge to developing constitutive hydraulic relationships required for modeling total system response. This study builds upon recent developments in modeling equilibrium liquid–vapor interfacial configurations in various pore spaces to provide approximate boundary conditions for introduction of hydrodynamic behavior. The media pore space is represented by a bimodal distribution of the two disparate populations of matrix pores and fracture apertures. Additionally, fracture surface roughness is represented by a distribution of angular pits and grooves. The model considers a cross-section in the FPM where liquid configurations take place in the plane, and steady flow takes place in the perpendicular direction (no lateral interactions are considered). In this study we focus on derivation of hydraulic conductivity of the fracture domain, and refer interested readers to a study by Tuller and Or [35] for details on matrix hydraulic conductivity functions.

Unlike the negligible role of the fracture domain in liquid retention behavior, flow in this domain dominates the hydraulic conductivity of the FPM near saturation. The composite unsaturated hydraulic conductivity function contains multiple "humps" representing at least three processes: (1) fracture flow (dominates under wet conditions); (2) matrix capillary flow (controls conductivity for intermediate wetness range); and (3) film flow (dry conditions). Aside from several conceptual limitations, the primary constraint to model testing and application is the lack of definitive data sets.

The 2-D analysis presented in this study relies on some measure of fracture aperture distribution, which is likely to be derived from image analysis, due to the limited information contained in fracture domain liquid retention. However, considering evidence suggesting that less than 20% of the fractures are water conducting [7,17], this casts some doubts on the direct use of such information. We are thus left with limited options with respect to reliable input data for the model, and the most robust input variable is a direct measurement of FPM saturated permeability. Critical path analysis offers an additional avenue for considerations of potential 3-D effects using fracture aperture distribution (rather the detailed 3-D network). The results reduce the problem to calculation of the saturated permeability of a "critical" unit fracture element.

In summarizing the results of this study, it is important to bear in mind several critical assumptions: (1) equilibrium between matrix and fracture domains; (2) flow occurs in parallel flow pathways perpendicular to the partially saturated FPM cross-section (no 3-D or cross flows considered); (3) interfacial configurations remain unchanged under slow and steady laminar flow; and (4) we do not consider rivulet flows and similar processes arising under strong dominance of gravitational forces.

The primary results of this study include (1) introduction of a new geometrical model for FPM pore space representation; (2) derivation of closed-form expressions for FPM liquid saturation, considering individual contributions of matrix and fracture domains; (3) derivation of physically based functions for prediction of FPM unsaturated hydraulic conductivity; (4) illustration of potential effects of non-equilibrium conditions between matrix and fractures on the unsaturated hydraulic conductivity function; and (5) introduction of potential strategies for inclusion of 3-D network effects via measured saturated permeability or CPA. Future work will focus on detailed experimental characterization of FPM properties to be used as input parameters for testing and refining the proposed model.

Acknowledgements

The authors gratefully acknowledge the partial support of the NSF under grant EAR-9805409, the USDA-NRI under grant 2001-35107-10181, the Nuclear Regulatory Commission (NRC) under contract no. NRC-02-97-009 to the Center for Nuclear Waste Regulatory Analysis (CNWRA), and the Idaho Agricultural Experimental Station (IAES). The authors thank the soil physics group at ETH Zürich for graciously sharing their data; in particular, we thank H. Flühler, U. Fischer, B. Kulli, and T. Gimmi for their assistance. This paper is an independent product of a contract to the CNWRA and does not necessarily reflect the view or regulatory position of the NRC. Approved as IAES journal paper no. 2719.

Appendix A. Average flow velocity in isosceles triangular surface grooves

A solution for average flow velocity in isosceles triangular ducts with a solid–liquid (no-slip) boundary at the legs of the triangle and a liquid–liquid boundary at the triangle base was derived using a finite difference-based numerical scheme. The results were generalized and expressed as:

$$\bar{v} = \zeta \frac{\tau^2 B^2}{\eta_0} \left(-\frac{\mathrm{d}P}{\mathrm{d}z} \right) \tag{A.1}$$

where ζ is a dimensionless flow resistance parameter dependent on the vertex angle (pit angle), η_0 is the liquid viscosity, and $\mathrm{d}P/\mathrm{d}z$ is the hydraulic head gradient in flow direction z. The relationship between flow resistance parameter ζ and pit angle γ may be parameterized as:

$$\zeta = 3.324 \times 10^{-4} + 6.057 \times 10^{-6}\gamma^2 - 1.963 \times 10^{-8}\gamma^3 \tag{A.2}$$

with γ in degree ($r^2 = 0.99998$). The validity of Eq. (A.2) and the solution for flow in corners bounded by a liquid–vapor interface [21,27,35] are limited to a range of pit angles of $30° \leqslant \gamma \leqslant 150°$, because of errors at very small and very large pit angles emerging from the applied numerical evaluation schemes.

Appendix B. Analytical solution for sample scale liquid saturation and hydraulic conductivity for the fracture domain

For all geometrical configurations with $\tau \geqslant \cos(\gamma/2)/(2\tan(\gamma/2))$ Eq. (4), we are able to obtain closed-form expressions for the sample-scale response of the fracture domain by multiplying the single element expressions for liquid saturation Eqs. (6) and (8) and hydraulic conductivity Eqs. (16) and (18) with the gamma distribution for aperture sizes, and integrating the resulting expressions over part of the fracture population associated with the different filling stages, as discussed in Section 2.2. The resulting integral equations may be expressed by the following general integral:

$$H = \int_{B_\mathrm{L}}^{B_\mathrm{U}} (c_1 B^4 + c_2 B^2 + c_3 B + c_4) \mathrm{Exp}\left[-\frac{B}{\omega} \right] \mathrm{d}B \tag{B.1}$$

where H represents the sample-scale hydraulic function, B_L and B_U are the lower and upper integration limits,

Table 4
Integration limits, constants, variables used to calculate sample scale liquid saturation, and saturated and unsaturated hydraulic conductivities for the fracture domain employing general Eq. (B.1)

	Lower integration limit B_L	Upper integration limit B_U	c_1	c_2	c_3	c_4
Degree of saturation						
S_1 complete saturation	B_{min}	$B_1(\mu)$	0	$\frac{1}{2\omega^3}$	0	0
$S_3(\mu)$ partially saturated	$B_1(\mu)$	B_{max}	0	0	$\frac{h(\mu)(2\tau+v\cos(\frac{\gamma}{2}))}{\omega^3[v\cos(\frac{\gamma}{2})+2\tau(1+\tau)\sin(\frac{\gamma}{2})]}$	$\frac{F_\gamma r(\mu)^2-2h(\mu)r(\mu)\cot(\frac{\gamma}{2})}{\omega^3[v+2\tau(1+\tau)\tan(\frac{\gamma}{2})]}$
Hydraulic conductivity						
K_{SAT} saturated conductivity	B_{min}	$B_1(\mu)$	$\frac{\phi_F[K_s(v+2\tau\tan(\frac{\gamma}{2}))+2K_d\tau^2\delta\tan(\frac{\gamma}{2})]}{2\omega^3[v+2\tau(1+\tau)\tan(\frac{\gamma}{2})]}$	0	0	0
K_2 (m) Unsaturated conductivity	$B_1(\mu)$	B_{max}	0	0	$\frac{\phi_F KF(\mu)h(\mu)(2\tau+v\cos(\frac{\gamma}{2}))}{\omega^3[v\cos(\frac{\gamma}{2})+2\tau(1+\tau)\tan(\frac{\gamma}{2})]}$	$\frac{\phi_F[KC(\mu)r(\mu)^2F_\gamma\delta-2KF(\mu)h(\mu)r(\mu)\cot(\frac{\gamma}{2})]}{\omega^3[v+2\tau(1+\tau)\tan(\frac{\gamma}{2})]}$

and c_1, c_2, c_3, and c_4 are constants or variables listed in Table 4. The analytical solution of the integral in Eq. (B.1) is given as:

$$H = F(B_L) - F(B_U) \tag{B.2}$$

with

$$F(B) = \omega\{e^{-B/\omega}[B(B^3c_1 + Bc_2 + c_3) + c_4 + \omega(4B^3c_1 + 2Bc_2 + c_3) + 2\omega^2(6B^2c_1 + c_2) + 24\omega^3Bc_1 + 24\omega^4c_1]\} \tag{B.3}$$

References

[1] Ambegaokar V, Halperin NI, Langer JS. Hopping conductivity in disordered systems. Phys Rev B 1971;4:2612–20.
[2] Banavar JR, Johnson DL. Characteristic pores sizes and transport in porous media. Phys Rev B 1987;35:7283–6.
[3] Bertels S, DiCarlo DA, Blunt MJ. Measurement of aperture distribution, capillary pressure, relative permeability, and in situ saturation in a rock fracture using computed tomography scanning. Water Resour Res 2001;37(3):649–62.
[4] Brown SR. Fluid flow through rock joints: The effect of surface roughness. J Geophys Res 1987;92(B2):1337–47.
[5] Brown SR, Kranz RL, Bonner BP. Correlations between the surfaces of natural rock joints. Geophys Res Lett 1986;13:1430–3.
[6] Chen Q, Kinzelbach W. An NMR study of single and two-phase flow in fault gauge filled fractures. J Hydrol 2002;259:236–45.
[7] Chiles JP, de Marsily G. Stochastic models of fracture systems and their use in flow and transport modeling. In: Bear J, Tsang Ch-F, de Marsily G, editors. Flow and contaminant transport in fractured rock. San Diego: Academic Press Inc.; 1993. p. 169–236.
[8] Dindoruk B, Firoozabadi A. Liquid film flow in a fracture between two porous blocks. Phys Fluids 1994;6(12):3861–9.
[9] Doyen PM. Permeability, conductivity and pore shape evolution of sandstone. J Geophys Res 1988;93:7729–40.
[10] Dury O, Fischer U, Schulin R. A comparison of relative nonwetting-phase permeability models. Water Resour Res 1999;35(5):1481–93.
[11] Fischer U, Kulli B, Flühler H. Constitutive relationships and pore structure of undisturbed fracture zone samples with cohesionless fault gauge layers. Water Resour Res 1998;34(7):1695–701.
[12] Friedman SP, Seaton NA. Critical path analysis of the relationship between permeability and electrical conductivity of three dimensional pore networks. Water Resour Res 1998;34(7):1703–10.
[13] Gimmi T, Schneebeli M, Flühler H, Wydler H, Baer T. Field-scale transport in unsaturated crystalline rock. Water Resour Res 1997;33(4):589–98.
[14] Glass RJ, Nicholl MJ, Tidwell VC. Challenging models for flow in unsaturated, fractured rock through exploration of small scale processes. Geophys Res Lett 1995;22:1457–60.
[15] Hunt A. Applications of percolation theory to porous media with distributed local conductances. Adv Water Res 2001;24:279–308.
[16] Kwicklis EM, Healy RW. Numerical investigation of steady liquid water flow in variably saturated fracture network. Water Resour Res 1993;29:4091–102.
[17] Liu HH, Doughty C, Bodvarsson GS. An active fracture model for unsaturated flow and transport in fractured rocks. Water Resour Res 1998;34(10):2633–46.
[18] Murphy JR, Thomson NR. Two-phase flow in a variable aperture fracture. Water Resour Res 1993;29(10):3453–76.

[19] Nicholl MJ, Rajaram H, Glass RJ. Factors controlling satiated relative permeability in a partially-saturated horizontal fracture. Geophys Res Lett 2000;27:393–6.
[20] Or D, Tuller M. Liquid retention and interfacial area in variably saturated porous media: upscaling from pore to sample scale model. Water Resour Res 1999;35(12):3591–605.
[21] Or D, Tuller M. Flow in unsaturated fractured porous media: hydraulic conductivity of rough surfaces. Water Resour Res 2000;36(5):1165–77.
[22] Perret J, Prasher SO, Kantzas A, Langford C. Three-dimensional quantification of macropore networks in undisturbed soil cores. Soil Sci Soc Am J 1999;63:1530–43.
[23] Persoff P, Pruess K. Two phase flow visualization and relative permeability measurement in rough-walled fractures. Water Resour Res 1995;31(5):1175–86.
[24] Pruess K, Narasimhan TN. On fluid reserves and production of superheated steam from fractured, vapor-dominated geothermal reservoir. J Geophys Res 1982;87(B11):9329–39.
[25] Pruess K, Tsang YW. On two-phase relative permeability and capillary pressure of rough-walled rock fractures. Water Resour Res 1990;26(9):1915–26.
[26] Pruess K, Faybishenko B, Bodvarsson GS. Alternative concepts and approaches for modeling flow and transport in thick unsaturated zones of fractured rocks. J Contam Hydrol 1999;38(1):281–322.
[27] Ransohoff TC, Radke CJ. Laminar flow of a wetting liquid along the corners of a predominantly gas-occupied noncircular pore. J Colloid Interf Sci 1988;121:392–401.
[28] Rice JA. Mathematical statistics and data analysis. 2nd ed. Belmont, CA: Duxbury Press; 1995.
[29] Sahimi M. Flow and transport in porous media and fractured rock: From classical methods to modern approaches, ISBN: 3527292608. New York: John Wiley & Sons; 1995.
[30] Soll W, Birdsell K. The influence of coatings and fills on flow in fractured, unsaturated tuff porous media systems. Water Resour Res 1998;34(2):193–202.
[31] Thoma SG, Gallegos DP, Smith DM. Impact of fracture coatings on fracture/matrix flow interactions in unsaturated, porous media. Water Resour Res 1992;28(5):1357–67.
[32] Tokunaga TK, Wan J. Water film flow along fracture surfaces of porous rock. Water Resour Res 1997;33(6):1287–95.
[33] Tsang YW, Tsang CF. Channel model of flow through fractured media. Water Resour Res 1987;23(3):467–79.
[34] Tuller M, Or D, Dudley LM. Adsorption and capillary condensation in porous media: liquid retention and interfacial configurations in angular pores. Water Resour Res 1999;35(7):1949–64.
[35] Tuller M, Or D. Hydraulic conductivity of variably saturated porous media—laminar film and corner flow in angular pore space. Water Resour Res 2001;37(5):1257–76.
[36] van Genuchten MT. A closed-form equation for predicting the hydraulic conductivity of unsaturated soils. Soil Sci Soc Am J 1980;44:892–8.
[37] Wang JSY, Narasimhan TN. Unsaturated flow in fractured porous media. In: Bear J, Tsang Ch-F, de Marsily G, editors. Flow and contaminant transport in fractured rock. San Diego: Academic Press Inc.; 1993. p. 325–94.